Natural compound 5,7,8-trimethoxyflavone mitigates radiation-induced lung injury by suppressing EMT and PI3K/Akt pathway

CUI-CUI GONG[1*], HUA-KANG LI[1*], YUAN-ZHEN MI[1], JUN-YANG CHEN[2], ZENG-YI FANG[3], SHUN-LIAN FU[1], LI QUAN[1], BING LIN[1], JIN-YI LANG[1-3], QIU CHEN[4], KE XU[2] and MEI-HUA CHEN[2,3]

[1]Chengdu University of Traditional Chinese Medicine, Chengdu, Sichuan 610032, P.R. China; [2]Department of Radiation Oncology, Radiation Oncology Key Laboratory of Sichuan Province, Sichuan Clinical Research Center for Cancer, Sichuan Cancer Hospital and Institute, Sichuan Cancer Center, Affiliated Cancer Hospital of University of Electronic Science and Technology of China, Chengdu, Sichuan 610041, P.R. China; [3]School of Medicine, University of Electronic Science and Technology of China, Chengdu, Sichuan 611731, P.R. China; [4]Department of Endocrine, Hospital of Chengdu University of Traditional Chinese Medicine, Chengdu, Sichuan 610075, P.R. China

Received August 29, 2025; Accepted December 22, 2025

DOI: 10.3892/ijmm.2026.5740

Abstract. Radiation-induced lung injury (RILI) remains a dose-limiting and life-threatening complication of thoracic radiotherapy. The present study aimed to evaluate the therapeutic efficacy and mechanism of the naturally extracted flavonoid, 5,7,8-trimethoxyflavone (HY-N7656), in inhibiting RILI. Lung injury in mice was evaluated using micro-computed tomography, histopathological analysis, enzyme-linked immunosorbent assay and western blotting. Network pharmacology was conducted to predict the potential therapeutic targets and signaling pathways of HY-N7656 in RILI. Cell Counting Kit-8, wound healing, immunofluorescence, reverse transcription-quantitative (RT-q) PCR and protein expression analyses were carried out *in vitro* using TGF-β-stimulated A549 cells to evaluate epithelial-mesenchymal transition (EMT) and signaling activity. Results of the present study revealed that HY-N7656 markedly alleviated pulmonary inflammation and fibrosis in irradiated mice, leading to a reduction in α-smooth muscle actin expression. In addition, EMT was effectively reversed following treatment with HY-N7656 in A549 alveolar epithelial cells treated with TGF-β, accompanied by restoration of E-cadherin expression and downregulation of mesenchymal markers, such as N-cadherin and vimentin. Network pharmacology analysis and molecular docking validation identified the PI3K/Akt pathway as a central target, which was subsequently confirmed via western blot analysis. Moreover, results of the present study demonstrated that HY-N7656 inhibited radiation-induced activation of PI3K and Akt. To the best of the authors' knowledge, the present study was the first to demonstrate that HY-N7656 modulates the PI3K/Akt signaling pathway to suppress the progression of EMT in RILI, establishing HY-N7656 as a multi-target inhibitor of RILI. These findings present a potential strategy to enhance the safety of radiotherapy, warranting further preclinical and clinical evaluation.

Correspondence to: Dr Mei-Hua Chen, Department of Radiation Oncology, Radiation Oncology Key Laboratory of Sichuan Province, Sichuan Clinical Research Center for Cancer, Sichuan Cancer Hospital and Institute, Sichuan Cancer Center, Affiliated Cancer Hospital of University of Electronic Science and Technology of China, 55 Section 4, Renmin South Road, Chengdu, Sichuan 610041, P.R. China
E-mail: chenmeihua@scszlyy.org.cn

*Contributed equally

Key words: radiation-induced lung injury, 5,7,8-trimethoxyflavone, epithelial-mesenchymal transition, PI3K/Akt, pulmonary fibrosis

Introduction

Radiotherapy remains a foundational treatment for thoracic malignancies (1,2); however, its efficacy is often compromised by radiation-induced lung injury (RILI) (3). This is a debilitating complication affecting 14.2% of patients receiving intensity-modulated radiotherapy (4) and 1.3% undergoing stereotactic radiotherapy (5). Characterized by progressive inflammation, fibrosis and respiratory failure (6), RILI not only limits radiation dose escalation, but also diminishes patient survival, with mortality rates >30% in severe cases (7). Current management relies heavily on glucocorticoids (8), which transiently alleviate symptoms but paradoxically increase infection risks and reduce tumor radiosensitivity (9,10). Given these limitations, it is imperative to develop novel therapeutic strategies that address the pathogenesis of RILI while maintaining anticancer effectiveness.

Results of a previous study indicated that the development of RILI is closely associated with epithelial-mesenchymal transition (EMT), a process in which alveolar epithelial cells lose their polarity, acquire mesenchymal-like properties and thereby contribute to fibrotic remodeling (11). TGF-β

plays a partial role in initiating EMT through triggering Smad-dependent signaling pathways and enhancing the production of mesenchymal proteins, including vimentin and α-smooth muscle actin (α-SMA) (12-17). Moreover, the PI3K/Akt signaling axis has been increasingly recognized for its role in intensifying EMT and contributing to fibrosis, through repressing E-cadherin expression via Snail and Twist regulation (18-20). Results of previous studies revealed that PI3K inhibitors may inhibit the proliferation and differentiation of lung fibroblasts into myofibroblasts (21). These results suggest that targeting the PI3K/Akt signaling pathway, which is involved in RILI, may serve as an effective strategy to attenuate radiation-induced EMT (22). Despite these advances, the precise mechanisms underlying the association between EMT and the PI3K/Akt pathway in the context of RILI remain to be fully elucidated.

Traditional Chinese Medicine includes a range of bioactive compounds with multi-target potential (23). Results of a previous clinical study demonstrate that patients treated with Huaxian Formula (HXF) experienced a markedly lower incidence of radiotherapy interruption due to severe RILI, compared with the control group (24). Moreover, results of previous *in vivo* studies confirm that HXF may act as a potent anti-RILI agent, reducing collagen deposition by 12.3% in murine models (25-27). Through serum pharmaco-chemistry and network pharmacology, HY-N7656 was isolated as the key active component of HXF, demonstrating the high binding affinity to PI3K/Akt targets (28). The flavonoid compound, HY-N7656, is a naturally derived product that has been investigated for multiple pharmacological activities, including anti-inflammatory, antioxidative, radioprotective and antifibrotic effects (23,29). Although HY-N7656 possesses the aforementioned pharmacological properties, the specific efficacy against RILI (30) and the potential involvement in the EMT process and PI3K/Akt signaling pathway remain unclear.

Thus, it was hypothesized that HY-N7656 may be among the first natural flavonoid compounds to attenuate RILI via dual inhibition of EMT and PI3K/Akt signaling. The establishment of a RILI model using C57BL/6 mice with whole-lung irradiation at 17 Gy is widely established, as it effectively replicates the key pathological and inflammatory features observed in human lungs (31,32). The present study aimed to investigate the potential protective effects of HY-N7656 in RILI both *in vitro* and *in vivo*, using TGF-β-stimulated alveolar epithelial cells and a murine RILI model. Subsequently, network pharmacology and molecular docking were used to explore the potential underlying mechanisms. Collectively, results of the present study indicated the potential role of HY-N7656 as a radiosensitizer-adjuvant, addressing a crucial gap in therapeutics targeting RILI.

Materials and methods

Animal experiments. C57BL/6 mice (SPF-grade; age, 8 weeks; weight, 20-25 g; n=80) were purchased from Beijing HFK Bio-Technology and used in all animal experiments. All animals were acclimatized for 7 days under standard conditions (22˚C; 50±10% relative humidity; 12 h light/dark cycle). To minimize sex-related variability in radiation response (30), only male mice were used. For experimental design, mice were randomized into four cohorts (20 per group), including a control group without treatment and an IR group receiving localized thoracic irradiation at 17 Gy. Efficacy dose selection was carried out and 15 mg/kg HY-N7656 was used for all experiments in order to limit toxicity and enhance therapeutic efficacy. Mice in the HY-N7656 (15 mg/kg) group were treated with irradiation and a daily intraperitoneal injection of 15 mg/kg HY-N7656. Mice in the drug-only group were treated with 15 mg/kg HY-N7656 without irradiation. On the second day following treatment initiation, mice were subjected to localized 60Co X-irradiation at a dose of 17 Gy (75 cGy/min), administered using a Precision X-Ray X-RAD 320 irradiator. Notably, non-target tissues of mice were protected using lead plates. HY-N7656 (purity, >99.9%; cat. no. 23050-38-6; TargetMol Chemicals Inc.) was administered intraperitoneally for 4 weeks post-irradiation and samples were collected from all mice at week 16 post-irradiation. In cases where severe distress or a weight loss >20% was observed, the mice were humanely sacrificed by cervical dislocation, in accordance with the guidelines set by the Animal Care and Use Committee (IACUC) to minimize suffering. Mice were anesthetized using isoflurane (3-4% for induction and 1.5-2% for maintenance) using an animal anesthesia system. Following anesthesia, 150-200 μl of orbital blood was collected from each mouse. Following blood collection, all animals were euthanized via cervical dislocation and death was confirmed by the absence of heartbeat and respiration for at least 2 min. The Animal Ethics Committee of Sichuan Cancer Hospital reviewed and approved all procedures involving animals (approval no. SCC HEC-04-2024-040).

Micro-computed tomography (CT) scan. At weeks 4, 8, 12 and 16 post-irradiation, mice were anesthetized using 2% isoflurane and scanned using a Quantum GX Micro-CT (Rigaku) with the following parameters: 80 kV, 100 μA, 360˚ rotation and 50 μm isotropic resolution. Lung density was quantified in Hounsfield units (HU) using 3D Slicer software (version 5.6.1; https://www.slicer.org), with healthy ventilation defined as -900 to -500 HU and impaired ventilation defined as -500 to -100 HU (33). CT scans were processed using 3D Slicer and lung HU values were quantified separately for each group.

Enzyme-linked immunosorbent assay (ELISA). In Week 16, serum levels of TGF-β were determined using a commercially available ELISA kit (cat. no. RK00057; ABclonal Biotech Co., Ltd.). Notably, orbital blood was collected and centrifuged at 1,000 x g for 20 min at 4˚C and the supernatant was extracted.

Histopathology and immunohistochemistry. Pulmonary samples were fixed in 10% neutral buffered formalin for 24 h at room temperature (20-25˚C), dehydrated through a graded ethanol series, cleared in xylene, paraffin-embedded, and sectioned at a thickness of 5 μm. Hematoxylin and eosin (H&E) staining was performed with hematoxylin for 5 min and eosin for 2 min at room temperature, and scoring was performed blindly according to the Szapiel criteria, which included the evaluation of alveolar wall thickness and inflammation (34). Masson's trichrome staining was performed at room temperature for a total duration of 60 min according to standard protocols, and fibrosis severity was subsequently assessed using Ashcroft scoring (35).

Immunohistochemical (IHC) staining for α-SMA was performed as follows: after antigen retrieval, sections were permeabilized with 0.1% Triton X-100 in PBS and then blocked with 5% non-fat milk at room temperature for 30 min. The primary antibody against α-SMA (cat. no. H660016003; Huabio) was diluted 1:5,000 and incubated at 4˚C for 16 h. Sections were subsequently incubated with an HRP-conjugated secondary antibody (cat. no. SA00001-1; 1:5,000; ProteinTech Group, Inc.) at room temperature for 30 min. After image acquisition using a light microscope, quantitative analysis of the positive staining area was performed using ImageJ 1.54p (National Institutes of Health).

Cell culture and HY-N7656 treatment. STR-verified A549 cells, derived from human lung adenocarcinoma, were cultured in DMEM (cat. no. PYG0073; Boster Biological Technology) containing 10% fetal bovine serum (cat. no. 40130ES; Shanghai Yeasen Biotechnology Co., Ltd.) at 37˚C with 5% CO_2 in a humidified incubator. Following overnight incubation in serum-free medium, cells were treated with or without HY-N7656 or TGF-β. Subsequently, the culture medium was exchanged for a serum-supplemented complete medium and cells underwent an additional 48-h incubation period.

Assessment of cell viability. A549 cell viability was evaluated utilizing Cell Counting Kit-8 (CCK-8; cat. no. 40203ES60; Shanghai Yeasen Biotechnology Co., Ltd.). Initially, cells were distributed into 96-well plates with each well containing $3x10^3$ cells. Following a 24-h incubation period at 37˚C, cells were treated with different concentrations of HY-N765 and cultured for a further 48 h at 37˚C. All cells were incubated with CCK-8 reagent and cell culture plates were incubated for 1 h at 37˚C. Optical density was measured at 450 nm and recorded with a Cytation 5 multimode cell imaging plate reader (BioTek; Agilent Technologies, Inc.).

Cell migration assay. A uniform monolayer of A549 cells was established in 6-well plates and the surface was scratched using a sterile 200-μl pipette tip. Residual debris was eliminated via washing with PBS. The cells were then treated with HY-N7656 (10 μM; cat. no. 23050-38-6; TargetMol Chemicals Inc.) and/or TGF-β (5 ng/ml; cat. no. 91701ES10; Shanghai Yeasen Biotechnology Co., Ltd.) in culture medium containing 0.5% FBS. Following 48 h of incubation with the specified treatments, three random fields corresponding to each scratch were selected and observed under a light microscope to assess cell migration. ImageJ 1.54p (National Institutes of Health) was used calculate wound healing, which was expressed as the percentage of the initial wound area covered during healing.

Immunofluorescence staining. A549 cells were seeded onto coverslips in 24-well plates at a density of $1.2x10^4$ cells per well. Following washing with PBS, A549 cells distributed in 24-well plates were fixed using 1 ml of 4% paraformaldehyde solution at room temperature for 20 mins. Cells were fixed, treated with 0.5% Triton X-100 to permeabilize membranes and rinsed using PBS. Subsequently, membranes were blocked using 5% BSA (cat. no. BSAS 1.0; Bovostar; Biovogen) for 1 h and incubated with the following primary antibodies at 4˚C overnight: Anti-E-cadherin (cat. no. 20874-1-AP; 1:500; ProteinTech Group, Inc.) and anti-vimentin (cat. no. 10366-1-AP; 1:1,000; ProteinTech Group, Inc.). Following washing with PBS, membranes were incubated with secondary antibodies for 30 min at room temperature: Fluorescein (FITC)-conjugated Goat Anti-Rabbit IgG(H+L) (cat. no. SA00003-2; 1:200; ProteinTech Group, Inc.) for red fluorescence and Goat Anti-Rabbit IgG H&L (Alexa Fluor® 488) (cat. no. ab150077; 1:200; Abcam) for green fluorescence. Cells were washed twice with PBS for 5 min each time and subsequently stained with DAPI for 10 min at room temperature in the dark. Fluorescent images were obtained at a magnification of x200 using a Nikon A1 confocal microscope with the addition of a laser scanner.

Network pharmacology and molecular docking analysis. To determine the potential targets of HY-N7656, data was integrated from multiple open-access databases, such as TCMSP, DrugBank, *SwissTargetPrediction* and *PharmMapper*. Genes associated with RILI were determined using multiple biomedical resources, including GeneCards, NCBI, OMIM and the DisGeNET platform. Duplicate entries were removed and an intersection analysis was conducted between the active compound targets and RILI-associated targets, followed by protein-protein interaction (PPI) analysis use the STRING database. To illustrate the interaction results, Cytoscape 3.9.0 (Cytoscape Consortium; https://cytoscape.org) was used for network mapping, followed by degree centrality (DC)-based identification of central targets (36). To gain further insights into the biological roles of the overlapping targets, functional enrichment analyses, including Gene Ontology (GO) and Kyoto Encyclopedia of Genes and Genomes (KEGG) enrichment analyses were conducted using the DAVID platform (https://david.ncifcrf.gov/). Following sorting according to gene quantity and significance level, data were visualized using an online tool provided by the Bioinformatics platform. PI3K and Akt protein structures were obtained from the Protein Data Bank (PDB) (https://www.rcsb.org/) and the mol2 structure of HY-N7656 was obtained from the ChemSpider database (https://www.chemspider.com/). Structures were imported into the CB-Dock2 online platform (https://cadd.labshare.cn/cb-dock2/) for molecular docking visualization (37). The relevant URLs for the databases are provided in Table SI.

Reverse transcription-quantitative (RT-q) PCR analysis. Total RNA was extracted from A549 cells seeded at a density of $8x10^4$ cells per well using the SteadyPure Quick Extraction kit (cat. no. AG21023; Accurate Biology) following the manufacturer's protocol. RNA concentration and purity were assessed using a NanoDrop 2000 spectrophotometer (Thermo Fisher Scientific, Inc.). Total RNA was reverse-transcribed into cDNA using the ExonScript RT SuperMix reverse transcription kit with dsDNase (cat. no. 231106-A5; Exongen) according to the manufacturer's protocol. qPCR analysis was conducted using UltraStart SYBR Green qPCR Master Mix (cat. no. 231008-A4; Exongen) on a CFX96 Real-Time system C1000™ thermal cycler (BioRad Laboratories, Inc.). The PCR cycling conditions consisted of an initial denaturation at 95˚C for 30 sec, followed by 40 cycles of denaturation at 95˚C for 5 sec and annealing/extension at 60˚C for 30 sec. Quantification of target gene mRNA was carried out using the $2^{-\Delta\Delta Cq}$ method based on comparative threshold cycles (38). Sequences of primers are listed in Table SII. All experiments were performed in triplicate.

Western blot analysis. Lung tissues and A549 cells were washed in pre-cooled PBS, lysed using RIPA lysis buffer (cat. no. PC101; Epizyme) and heated to 95˚C for denaturation. Protein concentration was determined using a BCA protein assay kit. Proteins were separated via electrophoresis on a 10% gel, with 30 μg of protein loaded per lane and transferred to a PVDF membranes. Subsequently, membranes were treated with 5% BSA for 1 h and incubated with the following primary antibodies overnight at 4˚C: Anti-E-cadherin (cat. no. 20874-1-AP; 1:2,000; ProteinTech Group, Inc.), anti-Vimentin (cat. no. 10366-1-AP; 1:2,000; ProteinTech Group, Inc.), anti-AKT (cat. no. ET1609-51; 1:2,000; Huabio), anti-phosphorylated (p)-AKT (cat. no. ab81283; 1:5,000; Abcam), anti-PI3K (cat. no. 251221; 1:2,000; ZenBio), anti-p-PI3K (cat. no. 341468; 1:2,000; ZenBio), anti-Ncadherin (cat. no. sc-525409; 1:1,000; Santa Cruz Biotechnology, Inc.) and anti-GAPDH (cat. no. AC002; 1:2,000; ABclonal Biotech Co., Ltd.). Following primary incubation, membranes were incubated with the following secondary antibodies for 1 h at room temperature: Goat anti-rabbit IgG (cat. no. AS014; 1:5,000; ABclonal Biotech Co., Ltd.) and goat anti-mouse IgG (cat. no. SA00001-1; 1:5,000; ProteinTech Group, Inc.). Proteins bands were visualized using an ultrasensitive ECL-based chemiluminescence assay (cat. no. RM02867; ABclonal Biotech Co., Ltd.) and expression was quantified using ImageJ software (version 1.54p; National Institutes of Health).

Statistical analysis. Statistical analysis was carried out using GraphPad Prism 9 (Dotmatics). Data are presented as the mean ± standard error of the mean (SEM). For statistical analysis, differences between two groups were analyzed using unpaired Student's t-tests following normality testing, while one-way ANOVA followed by Tukey's post-hoc test was used for comparisons between multiple groups. Investigators were blinded during histological scoring and data analysis to eliminate any potential bias. The scoring results were analyzed using the nonparametric Kruskal-Wallis test followed by Dunn's post-hoc test. $P<0.05$ was considered to indicate a statistically significant difference.

Results

HY-N7656 dose optimization and survival benefits in RILI mice. Mice in the RILI model received HY-N7656 intraperitoneally at doses of 7.5, 15 and 30 mg/kg, corresponding to low, medium and high concentrations. The results revealed that all three doses alleviated the radiation-induced increase in lung density and reduced pulmonary pathological changes (Fig. 1A). As displayed in Fig. 1B, the rate of increase in lung density gradually decreased from 47.7 to 34.7 and 30.9% with increasing drug dosage, compared with the control group. Relative to the IR group, treatment with HY-N7656 at a dose of 7.5 mg/kg led to a 10.9% reduction in the lung density values of mice. For the 15 and 30 mg/kg dosages, the decreases in lung density values were recorded as 23.9 and 27.7%, respectively. The pathological scoring results displayed in Fig. 1C revealed that, compared to the control group, the effects of the low dose ($P<0.001$) were significantly lower than those of the medium and high doses ($P<0.0001$). Compared with the 15 mg/kg dose, the 30 mg/kg dose showed a trend toward improved efficacy; however, statistical analysis revealed no significant difference between the two ($P>0.05$). Accordingly, 15 mg/kg was selected as the optimal dose for subsequent experiments. During the 16-week period following irradiation, multiple parameters were monitored to evaluate the therapeutic efficacy of HY-N7656 on RILI in mice. As shown in Fig. S1A, compared with the control group, the fur in the irradiated chest region progressively changed from black to gray-white by Week 16. Whole-chest irradiation resulted in high mortality and survival status in each group was recorded at Week 16. The HY-N7656+IR group exhibited a survival benefit at Week 4 and a prolonged survival advantage was maintained over time, with a higher survival rate (60%) compared with the irradiated group alone (20%), using the control group as the baseline (Fig. S1B). Of the 20 irradiated mice, 75% (15 mice) died, while 5 survived to 16 weeks, consistent with previous reports on thoracic irradiation lethality (39,40). Based on our previous studies (27,28), 5 mice per group were considered sufficient to obtain statistically significant results. Body weight was also monitored as an indicator of general health. As shown in Fig. S1C, mice in the IR group exhibited a weight loss of 29.2% compared with the control group ($P<0.0001$), whereas HY-N7656 treatment led to a weight loss of 14.9% ($P<0.001$). Collectively, these findings indicated that prophylactic administration of HY-N7656 markedly reduced radiation-induced mortality in mice and improved their overall health status.

HY-N7656 preserves lung architecture and reduces fibrosis. The experimental procedure for animal experiments is outlined in Fig. 2A. As illustrated in Fig. 2B, longitudinal micro-CT imaging of the irradiated group at 4, 8, 12 and 16 weeks revealed progressive damage in the lungs of the IR group. Radiological examination at 16 weeks demonstrated classical fibrotic indicators, including distorted septal architecture, peripheral reticular densities and honeycomb-like lesions. Notably, HY-N7656 intervention markedly alleviated these morphological signs of RILI in treated mice. A computational assessment of HU values was carried out to determine alterations in lung parenchymal density following radiation exposure. In the IR group, high-density foci were observed in the lungs after 8 weeks, with a significant increase in lung density 16 weeks post-irradiation (Fig. 2D). Lung densitometric progression was reduced by 27.6% in mice receiving HY-N7656 and the results were statistically significant ($P<0.001$).

At 16 weeks post-irradiation, tissues were collected for morphological analysis and the results confirmed that all organs, including the heart, liver, spleen and kidneys, remained visibly healthy across all groups, excluding the lungs (Fig. S2). Lung tissue sections stained with H&E exhibited a healthy pulmonary morphology in both the HY-N7656 and control groups, with open alveolar spaces and no evidence of inflammatory cell infiltration. Significant histopathological alterations were detected in the IR group, with features such as alveolar collapse, interstitial edema, inflammatory cell accumulation and thickening of the alveolar septa. Lung tissues obtained from the IR+HY-N7656 group exhibited attenuated pathological changes, including alleviation of alveolar septal thickening and suppression of immune cell infiltration (Fig. 2C). According to the Szapiel criteria, the IR group exhibited markedly elevated inflammation

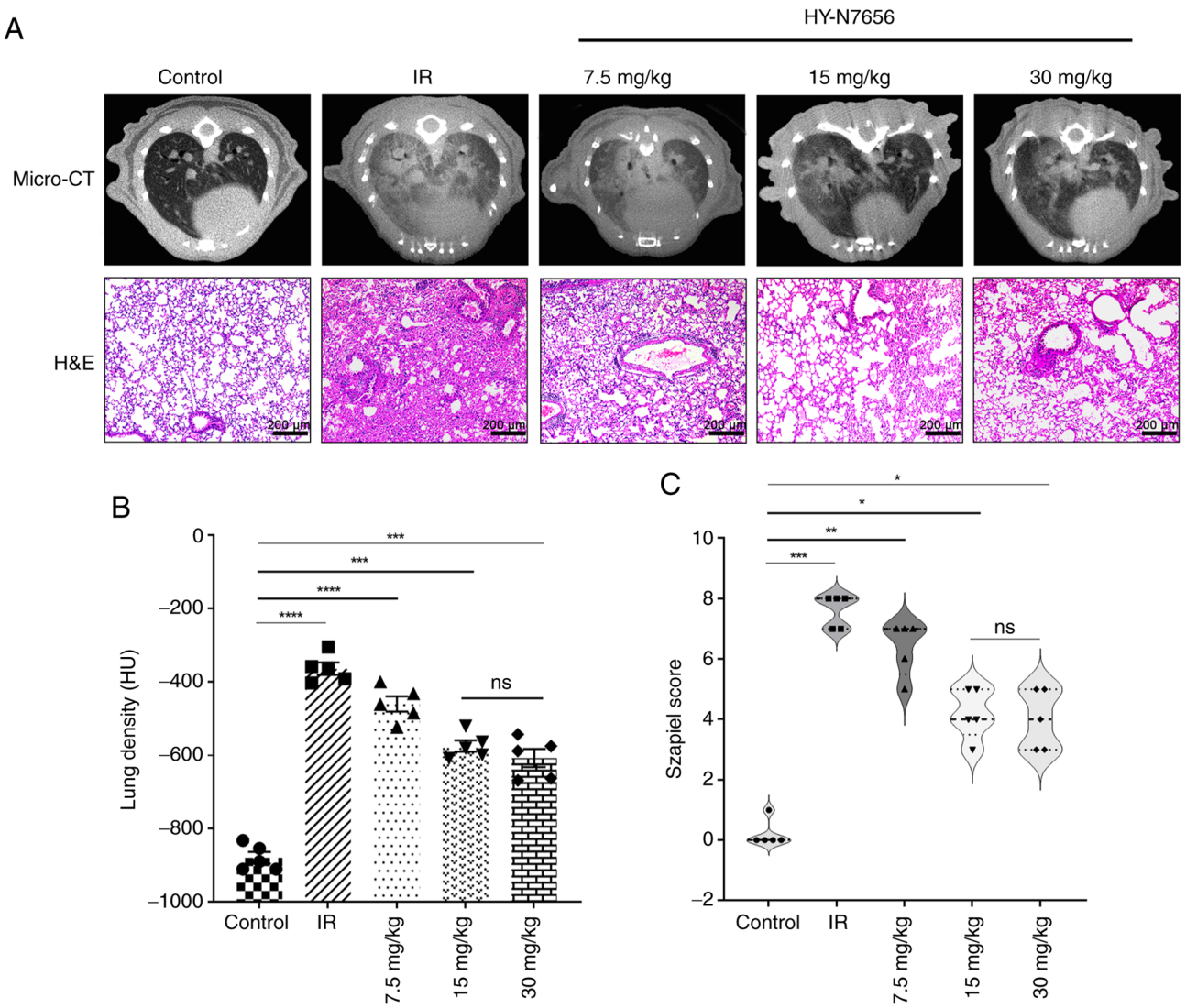

Figure 1. Effect of HY-N7656 on lung injury in an IR-induced model. (A) Micro-CT images and H&E-stained lung tissue sections from mice in the Control, IR and HY-N7656 treatment groups (7.5, 15 and 30 mg/kg). Magnification, x100. Scale bar, 200 μm. (B) Quantification of lung density (HU) based on micro-CT imaging demonstrated a significant decrease in lung density in the IR group relative to the control group, with HY-N7656 producing a dose-dependent improvement. (C) Histopathological scoring (Szapiel score) demonstrated a significant reduction in tissue damage in HY-N7656-treated mice compared with the IR group. Data are presented as mean ± SEM (n=5). *P<0.05, **P<0.01, ***P<0.001, ****P<0.0001; ns, no significance. HY-N7656, 5,7,8-trimethoxyflavone; IR, ionizing radiation; HU, Hounsfield unit; micro-CT, micro-computed tomography; H&E, haematoxylin and eosin; SEM, standard error of the mean.

scores relative to both the control and HY-N7656-only groups (P<0.0001). Notably, the IR + HY-N7656 group exhibited a reduction of >50% in lung inflammation score, compared with the IR group (P<0.01; Fig. 2E). Collagen accumulation in lung tissue was assessed using Masson's trichrome staining. The findings indicated that lung structure appeared healthy in both the HY-N7656 and control groups. Compared with the control group, the IR group demonstrated pathological evidence of fibrosis, characterized by substantial extracellular matrix accumulation. Relative to the IR group, lungs obtained from the IR + HY-N7656 group exhibited suppressed extracellular matrix deposition and reduced fibrotic severity. The Ashcroft score further indicated that HY-N7656 inhibited the radiation-induced increase in score by 27% (Fig. 2F).

To further examine the role of HY-N7656 in modulating fibrosis, a marker associated with RILI; namely α-SMA, was analyzed via immunohistochemistry. Results of the present study highlighted that the levels of α-SMA in lung tissue increased by 4.7-fold from baseline following irradiation, while HY-N7656 treatment effectively reduced α-SMA levels to 2.7 times the expected level, thereby alleviating radiation-induced myofibroblast differentiation (P<0.001; Fig. 2G). Collectively, these observations demonstrated that HY-N7656 may alleviate pulmonary damage following radiation exposure by dampening inflammatory processes and inhibiting extracellular matrix deposition.

HY-N7656 inhibits RILI progression via suppression of EMT in vivo. As illustrated in Fig. 3A, circulating TGF-β levels in irradiated mice increased by 110.8 pg/ml (2.8-fold) compared with the control group (P<0.0001). By contrast, HY-N7656 treatment attenuated this radiation-induced elevation by 1.2-fold relative to the IR group, further supporting the compound anti-RILI effects of HY-N7656. Blood parameters (Fig. S3) and liver and kidney function indices (Fig. S4) remained within expected ranges in all groups, confirming the

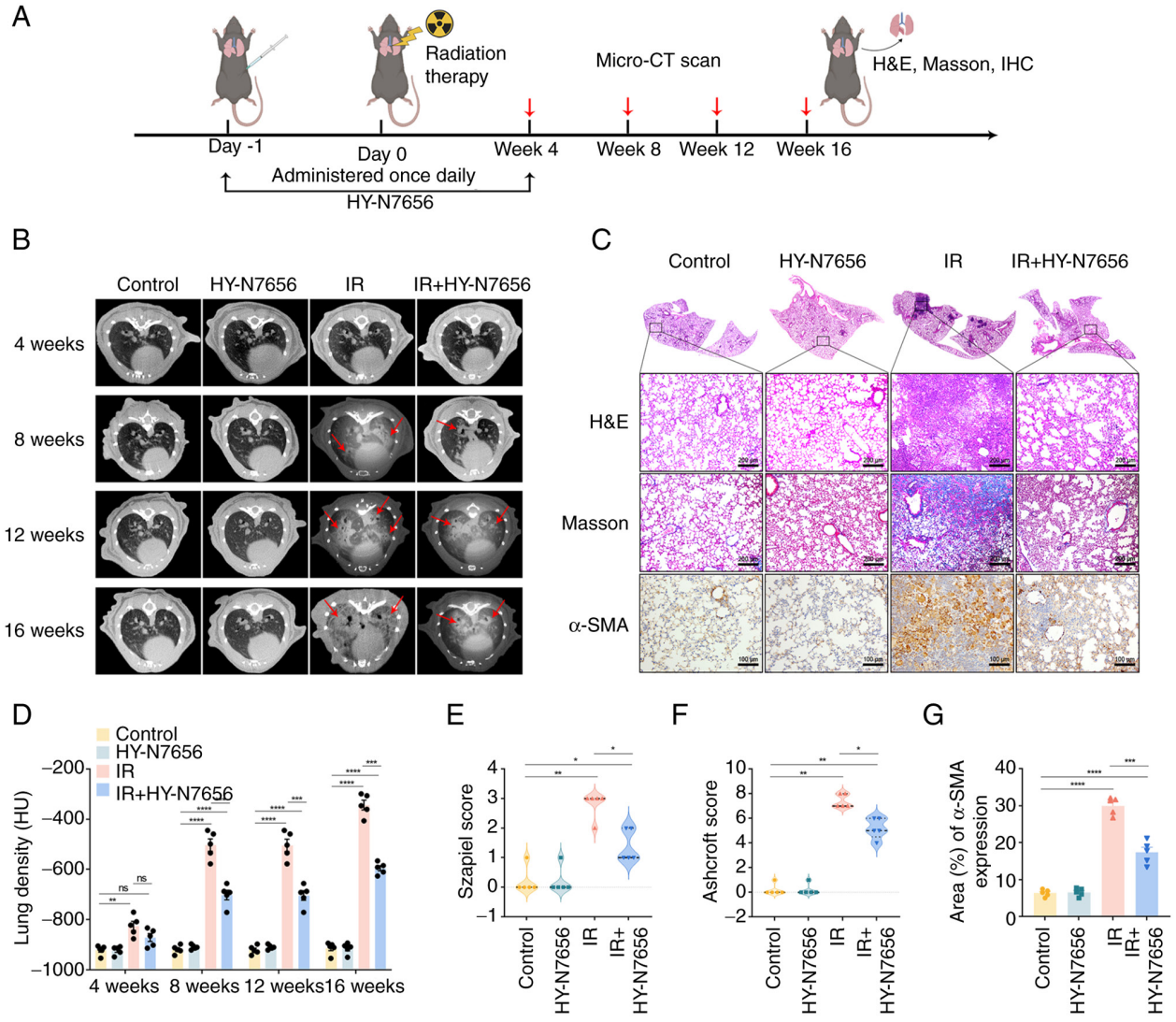

Figure 2. Effects of HY-N7656 on lung morphology and histopathological changes in irradiated mice. (A) Experimental design showing the timeline of radiation therapy, HY-N7656 administration and evaluation at Weeks 4, 8, 12 and 16 through micro-CT scan, H&E staining, Masson staining and IHC analysis. (B) Representative micro-CT images of lung morphology at 4, 8, 12 and 16 weeks post-treatment. Radiation-induced lung injury is indicated by arrows. (C) Representative histological analysis of lung tissue at 16 weeks. H&E, Masson (magnification, x100; scale bar, 200 μm) and α-SMA staining (magnification, x200; scale bar, 100 μm) revealed progressive fibrosis in the IR group, while HY-N7656 treatment reduced fibrosis and α-SMA expression, indicating a protective effect. (D) Quantification of lung density (HU) based on micro-CT imaging at each time point showed significant improvement in lung density in HY-N7656-treated groups compared with the IR group. (E) Szapiel score for H&E staining in lung tissue sections. (F) Ashcroft score for Masson staining in lung tissue sections. (G) Quantification of α-SMA-positive area (%) in lung tissue. Data are presented as mean ± SEM (n=5), *P<0.05, **P<0.01, ***P<0.001, ****P<0.0001, ns, no significance. HY-N7656, 5,7,8-trimethoxyflavone; IR, ionizing radiation; HU, Hounsfield unit; micro-CT, micro-computed tomography; H&E, hematoxylin and eosin; IHC, immunohistochemistry; α-SMA, α-smooth muscle actin; SEM, standard error of the mean.

biosafety of HY-N7656. The lung index (lung-to-body-weight ratio), an indicator of pulmonary edema, was markedly elevated in irradiated mice compared with controls (Fig. 3B). HY-N7656 markedly mitigated this increase, reducing the lung coefficient by 73.4% and bringing it closer to physiological levels (P<0.001). Consistent with these findings, hydroxyproline content in lung tissue at 16 weeks post-irradiation was elevated 2.6-fold in the IR group, whereas HY-N7656 limited this increase to 1-fold, effectively suppressing radiation-induced collagen accumulation (P<0.001; Fig. 3C). Results of a previous study demonstrate that EMT plays a key role in the progression of radiation-induced pulmonary fibrosis (41). To further validate results of the *in vivo* studies, the expression levels of EMT-associated proteins in mouse lung tissues were investigated. Western blot analysis confirmed that HY-N7656 effectively reversed radiation-induced EMT (Fig. 3D). Specifically, E-cadherin, an epithelial marker that was markedly downregulated following irradiation, was restored to twice its irradiated level following HY-N7656 treatment (P<0.05; Fig. 3E). Moreover, HY-N7656 reduced the irradiation-induced upregulation of the mesenchymal marker vimentin by 33.9%, with the final expression level being comparable to that of the control group (P>0.05; Fig. 3F). Collectively, these results highlighted the protective effects of HY-N7656 against radiation-induced pulmonary injury and further supported its translational potential in preclinical models.

HY-N7656 alleviates TGF-β-induced cellular EMT. A safe working concentration range for HY-N7656 was first

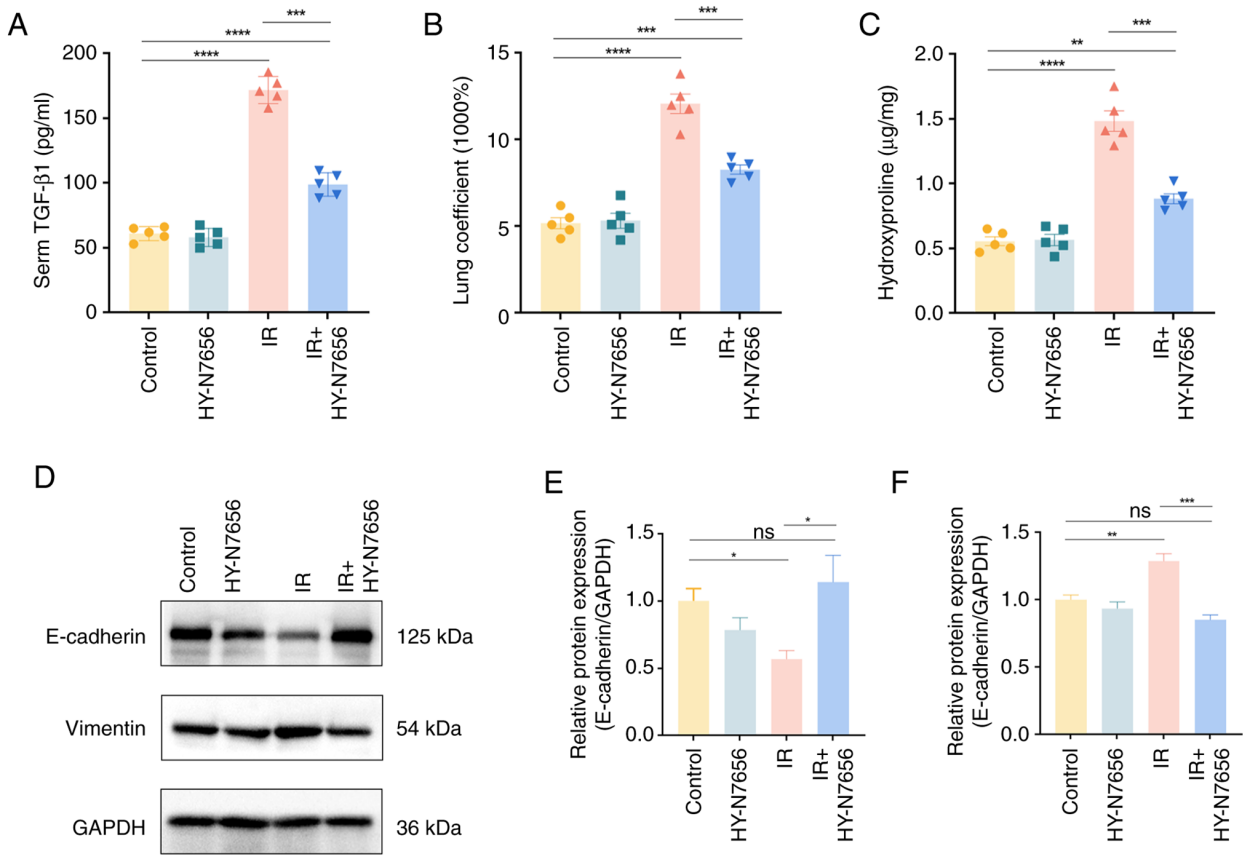

Figure 3. HY-N7656-mediated inhibition of RILI and associated mechanisms in irradiated mice. (A) Detection of serum TGF-β levels using ELISA at 16 weeks post-irradiation in each group of mice (n=5). (B) Statistical analysis of relative lung coefficient in each group of mice (n=5). (C) Quantification of hydroxyproline content in lung tissues at 16 weeks post-radiation (n=5). (D) Western blot analysis of EMT markers in RILI mice at 16 weeks post-irradiation. Quantification of (E) E-cadherin and (F) vimentin protein expression levels. Data are presented as mean ± SEM, *P<0.05, **P<0.01, ***P<0.001, ****P<0.0001, ns: no significance. HY-N7656, 5,7,8-trimethoxyflavone; RILI, radiation-induced lung injury; TGF-β, transforming growth factor-β; ELISA, enzyme-linked immunosorbent assay; EMT, epithelial-mesenchymal transition; SEM, standard error of the mean; ns, not significant.

determined using the CCK-8 assay. A549 cells, representing human alveolar type II epithelial cells, were exposed to HY-N7656 at 5-30 μM and cell viability was assessed at 24 and 48 h (Fig. S5A and B). Based on these results, 5, 10 and 20 μM were selected as safe intervention concentrations for subsequent experiments. In the TGF-β-induced A549 fibrosis model, HY-N7656 was used at these doses. Notably, 10 μM HY-N7656 (Fig. S6B) elicited the most robust anti-fibrotic response, markedly downregulating EMT markers; namely, N-cadherin and vimentin, while restoring E-cadherin expression levels, compared with 5 μM (Fig. S6A) and 20 μM (Fig. S6C).

EMT is a key process through which epithelial cells acquire mesenchymal characteristics. Upon TGF-β stimulation, A549 cells underwent a marked morphological transition, from orderly cobblestone-like epithelial cells to elongated mesenchymal-like cells with reduced intercellular adhesion. HY-N7656 effectively prevented these morphological changes, helping to preserve the epithelial phenotype (Fig. S7). To further assess the effect of HY-N7656 on cell motility, a wound healing assay was performed. TGF-β markedly enhanced A549 cell migration over 48 h; however, compared to the IR group, HY-N7656 reduced this increase from 2.5- to 1.6-fold (P<0.001), demonstrating a significant inhibitory effect on migration (Fig. 4A and B).

Notably, E-cadherin is essential for maintaining epithelial integrity and its loss is a hallmark of EMT and vimentin is strongly upregulated during the mesenchymal transition. Thus, expression levels were examined using immunofluorescence staining in the TGF-β-induced model (Fig. 4C and D). Results of the present analysis revealed that, compared to the IR group, TGF-β reduced intracellular E-cadherin to 40% of control levels, whereas HY-N7656 increased expression to 77% of expected levels. Conversely, HY-N7656 decreased aberrant vimentin expression by 16.3% (P<0.001; Fig. S8A and B).

Radiation-induced EMT disrupts epithelial polarity, cell-cell adhesion and cytoskeletal structure. To further clarify the mechanism by which HY-N7656 mitigates EMT, western blot analysis was performed (Fig. 4E). Results of the present study revealed that HY-N7656 suppressed TGF-β-induced N-cadherin upregulation, limiting its increase to 40% (P<0.001), reduced vimentin expression by 24.6% (P<0.05) and attenuated E-cadherin downregulation by 36.8% (P<0.05; Fig. 4F-H). Overall, these findings demonstrated that HY-N7656 effectively inhibited TGF-β-induced EMT *in vitro*, reduced cell migration and preserved epithelial phenotype, highlighting its therapeutic potential in preventing fibrosis-associated cellular reprogramming.

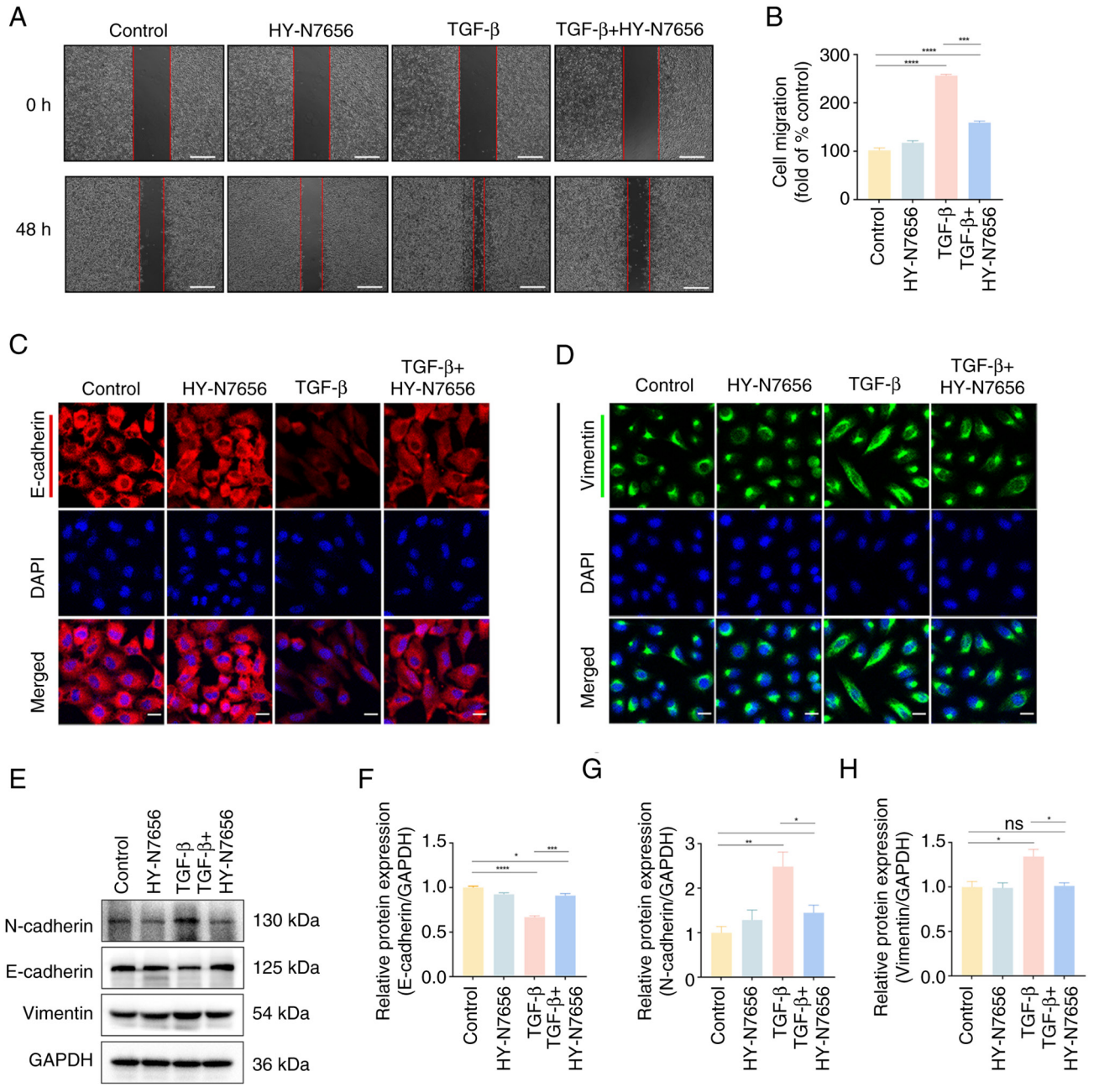

Figure 4. The effect of HY-N7656 on cell migration and EMT markers. (A) Representative images of wound healing assays highlighting cell migration at 0 and 48 h after treatment in control, HY-N7656, TGF-β and TGF-β + HY-N7656 groups. The red lines indicate the wound area (scale bar, 500 μm). (B) Quantification of cell migration represented as fold change relative to control. (C) Immunofluorescence staining of E-cadherin (red) and DAPI (blue) in A549 cells (scale bar, 20 μm). (D) Immunofluorescence staining of vimentin (green) and DAPI (blue) in A549 cells (scale bar, 20 μm). (E) Western blot analysis of N-cadherin, E-cadherin and vimentin protein expression levels in cells. GAPDH was used as a loading control. Quantification of (F) E-cadherin, (G) N-cadherin and (H) vimentin protein expression. Data are presented as mean ± SEM (n=3), *P<0.05, **P<0.01, ***P<0.001, ****P<0.0001, ns, not significant. HY-N7656, 5,7,8-trimethoxyflavone; EMT, epithelial-mesenchymal transition; TGF-β, transforming growth factor-β; DAPI, 4',6-diamidino-2-phenylindole; GAPDH, glyceraldehyde 3-phosphate dehydrogenase; SEM, standard error of the mean.

Network pharmacology and molecular docking analysis. As displayed in Fig. 5A, 58 overlapping target genes were identified between 118 HY-N7656- and 1,712 RILI-associated targets. The PPI network constructed via STRING and visualized in Cytoscape 3.9.0 revealed six hub genes; namely, ALB, EGFR, MMP9, PTGS2, ESR1 and SRC, through CytoNCA centrality analysis (Fig. 5B). Previous studies demonstrated that targeting the aforementioned pathways may improve DNA repair, inflammatory responses and apoptosis in irradiated cells, thereby protecting lung tissue from radiation toxicity and potentially enhancing the efficacy of radiotherapy (42-46). As displayed in Fig. 5C, GO enrichment analysis indicated that these targets mainly regulate biological processes associated with oxidative stress, inflammation and cell proliferation (Table SIII). KEGG analysis further revealed significant enrichment of multiple signaling pathways, including the PI3K/Akt pathway (Fig. 5D; Table SIV), suggesting that this may be a potential core mechanism underlying the therapeutic effects of HY-N7656 in the treatment of RILI. Fig. 5E and F illustrate the docking visualization between the small

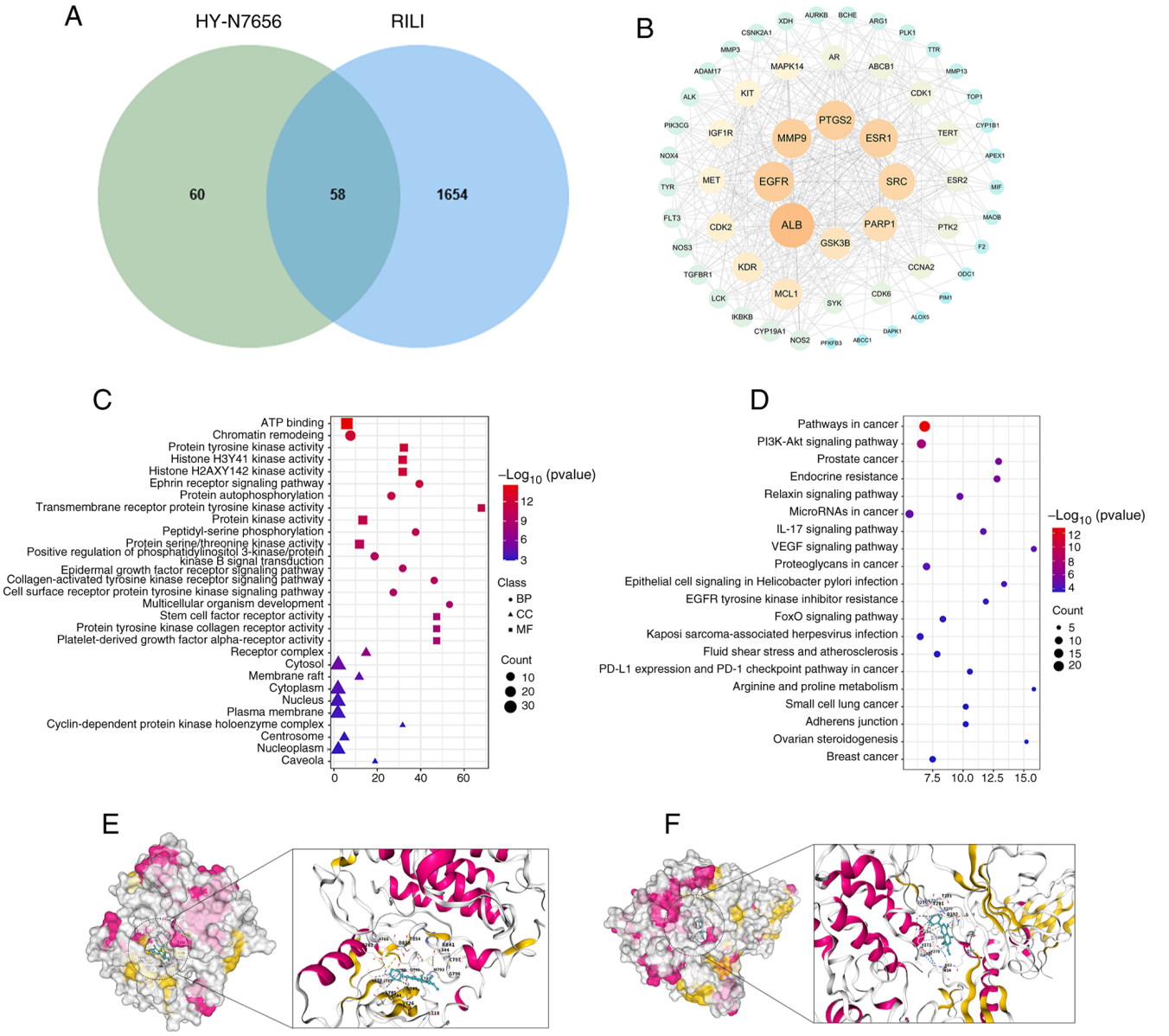

Figure 5. Network pharmacology analysis. (A) After intersecting 118 targets of HY-N7656 with 1,712 RILI-related targets, 58 common targets of HY-N7656 acting on RILI were identified. (B) PPI network diagram of the 58 intersecting targets, with node importance decreasing from large to small and color transitioning from yellow to green. (C) GO enrichment of HY-N7656 targets for the treatment of RILI, highlighting the top 10 enriched BPs, CCs and MFs. (D) Top 20 KEGG pathways enriched for HY-N7656 in the treatment of RILI. (E) Visualization of molecular docking between HY-N7656 and PI3K. (F) Visualization of molecular docking between HY-N7656 and Akt. HY-N7656, 5,7,8-trimethoxyflavone; RILI, radiation-induced lung injury; PPI, protein-protein interaction; GO, Gene Ontology; BP, biological process; CC, cellular component; MF, molecular function; KEGG, Kyoto Encyclopedia of Genes and Genomes; PI3K, phosphoinositide 3-kinase.

molecule compound, HY-N7656 and PI3K and Akt proteins, with binding energies of -7.3 and -9.4 kcal/mol, respectively. These results highlighted a strong binding affinity between HY-N7656 and PI3K/Akt, meaning HY-N7656 may exert its therapeutic effects through targeting the PI3K/Akt signaling pathway. These findings may provide a validation basis for further mechanistic studies of HY-N7656.

HY-N7656 inhibits the PI3K/Akt pathway. Based on the previous KEGG pathway enrichment analysis using network pharmacology, the PI3K/Akt axis may serve as a critical mechanism by which HY-N7656 exerts its inhibitory effect on RILI. Results of the western blot analysis revealed that Akt and PI3K phosphorylation levels were upregulated by ~1.6- and 1.8-fold, respectively, following treatment with TGF-β, compared with the control group ($P<0.05$ and $P<0.001$; Fig. 6A-C). Notably, a significant decline in phosphorylated (p)-Akt and p-PI3K levels was observed following treatment with HY-N7656, with reductions of 32.8 and 45.6%, respectively. Thus, HY-N7656 inhibited the PI3K/Akt signaling triggered by TGF-β and this inhibitory effect was associated with the suppression of EMT progression. A schematic diagram of the effect of HY-N7656 on RILI is displayed in Fig. 6D.

Discussion

RILI is a well-recognized complication of radiotherapy for thoracic tumors (47-49), ultimately leading to impaired lung function, respiratory failure and, in some cases, mortality (50). Despite its clinical severity, effective strategies for preventing

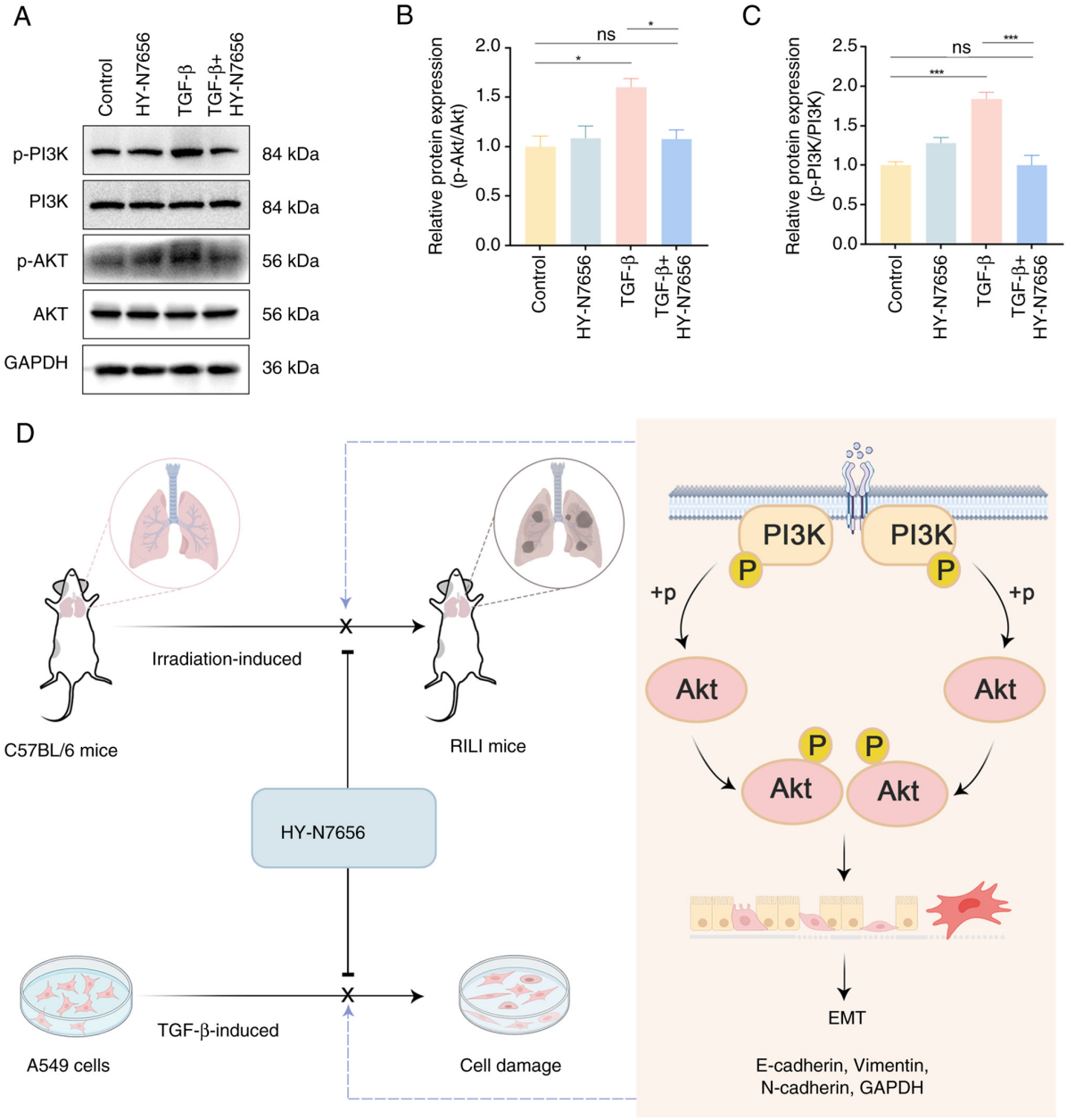

Figure 6. HY-N7656 inhibits activation of the PI3K/Akt signaling pathway in A549 cells. (A) Western blot analysis of PI3K, AKT, PI3K phosphorylation and AKT phosphorylation in A549 cells. Quantitative analysis of (B) p-Akt and (C) p-PI3K protein levels. GAPDH was used as the loading control. Data are presented as mean ± SEM. *P<0.05, ***P<0.001. (D) Mechanism of action for HY-N7656 in alleviating RILI via inhibition of PI3K/Akt mediated partial EMT. HY-N7656, 5,7,8-trimethoxyflavone; PI3K, phosphoinositide 3-kinase; AKT, protein kinase B; RILI, radiation-induced lung injury; EMT, epithelial-mesenchymal transition; GAPDH, glyceraldehyde 3-phosphate dehydrogenase; SEM, standard error of the mean; p-, phosphorylated.

and managing RILI remain limited, highlighting the requirement for novel therapeutic interventions. A previous study demonstrated that the natural flavonoid, HY-N7656, possesses anti-inflammatory activity (29). In the present study, HY-N7656 was identified as a first-in-class dual inhibitor of EMT and PI3K/Akt signaling, offering a mechanistically novel approach for the treatment of RILI. The findings demonstrated that early administration of HY-N7656 effectively inhibited the progression of RILI.

The progression of RILI is strongly associated with EMT, which functions as a fundamental mechanistic pathway (51). Results of a previous study demonstrated that oral administration of the heat shock protein 70 inducer geranylgeranylacetone in irradiated mice sustains E-cadherin expression and suppresses EMT markers, thereby exerting protective effects against RILI (52). Emetine dihydrochloride has similarly been reported to reduce EMT-associated markers and decrease Smad3 phosphorylation, mitigating RILI through EMT inhibition (53). Across diverse contexts, EMT is characterized by shared regulatory features, including alterations in cell morphology, increased cell motility, loss of epithelial traits and acquisition of mesenchymal properties (54). Consistent with previous findings (55,56), thoracic irradiation in mice was confirmed to induce pulmonary EMT, as indicated by reduced epithelial polarity, reduced E-cadherin expression, impaired intercellular junctions and increased vimentin levels. TGF-β is widely recognized as a key driver of EMT (57) and acts as a major upstream regulator in the initiation of acute lung inflammation, as well

as the progression of chronic fibrosis (13). Given its central role in RILI-associated pulmonary fibrosis, inhibition of TGF-β activation and expression is considered an effective strategy for slowing RILI progression. For example, Jiawei Maxing Shigan Tang, a traditional Chinese herbal formula, has been reported to improve RILI outcomes, potentially via the modulation of Tregs, inhibiting the TGF-β/Smad axis and attenuating EMT-associated processes (58). In the present study, HY-N7656 treatment restored E-cadherin levels in lung tissue, reduced vimentin expression and effectively inhibited radiation-induced EMT. Further experiments indicated that this effect was attributable to suppression of TGF-β elevation during RILI. These findings demonstrated that HY-N7656 improves RILI through the inhibition of TGF-β-induced EMT progression.

Network pharmacology analysis revealed that the PI3K/Akt signaling pathway was markedly enriched. As one of the most frequently activated pathways in RILI, this finding suggested that HY-N7656 may exert its therapeutic effects through this axis, warranting further investigation. Subsequent molecular docking validation indicated that HY-N7656 possesses a strong binding association with key components of the PI3K/Akt signaling pathway. In addition to canonical TGF-β signaling, aberrant activation of the PI3K-Akt pathway plays a critical role in driving EMT initiation and promoting tissue structural alterations (59,60). At elevated levels, TGF-β activates the PI3K/Akt signaling pathway, which subsequently downregulates FOXO3a expression; thus, inducing EMT in alveolar epithelial cells (61). This pathway is frequently emphasized in studies of cancer, inflammation and fibrosis (62). AKT, the principal downstream effector of PI3K, exhibits markedly increased phosphorylation following radiation exposure. Results of a previous study demonstrated that targeting the AKT/GSK3β signaling pathway effectively attenuated radiation-induced EMT in alveolar epithelial cells, offering a potential therapeutic strategy for RILI (63).

Akt signaling facilitates EMT progression through the suppression of Snail and Twist, transcription factors that regulate E-cadherin (64). For example, Myrtol reduces phosphorylated AKT expression and enhances E-cadherin levels, thereby inhibiting EMT and providing protective effects against RILI (65). Results of a previous study demonstrate that Akt inhibitors decreased E-cadherin and elevated α-SMA expression, further highlighting the role of the PI3K/Akt pathway in promoting EMT progression (22). Moreover, Re-Du-Ning, a formulation derived from *Artemisia* and its bioactive constituents, has been reported to mitigate RILI through inhibition of PI3K/Akt signaling and suppression of EMT progression (66). This highlights the PI3K/Akt pathway as a potential target for EMT inhibition (67). Results of a previous study also demonstrates that low molecular weight fucose may attenuate EMT and fibrotic remodeling through modulation of PI3K/Akt pathway activity in both *in vivo* and *in vitro* models (68). Collectively, this evidence supports the hypothesis that PI3K phosphorylation-induced Akt signaling plays a central role in activating EMT in AT2 cells, establishing the PI3K/Akt pathway as an effective and strategic target for RILI intervention. *In vitro* experimental data further confirmed that HY-N7656 effectively blocks transmission through the PI3K/Akt signaling pathway, thereby suppressing EMT progression in the context of RILI. Compared with compounds, such as Myrtol and emetine, which mitigate EMT in RILI, HY-N7656 more precisely delineates the PI3K/Akt pathway as a critical therapeutic target, demonstrating distinct mechanistic advantages.

However, the present study exhibits limitations. For example, results from the initial experiments of the present study demonstrated that a 15 mg/kg dose of HY-N7656 effectively prevents and treats RILI. Although associated pathological and biochemical experiments have confirmed the safety of HY-N7656, pharmacokinetic evaluation remains indispensable for future clinical translation. In addition, inclusion of female mice alongside male mice will be required in future work to address the limitation of using only male mice in the present study. Molecular docking and associated experimental evidence demonstrated that HY-N7656 inhibited RILI through the PI3K/Akt signaling pathway. However, it has not yet been determined whether HY-N7656 also exerts effects on radiation-activated Wnt/β-catenin and NF-κB signaling pathways, which promote lung fibrosis and inflammation (69,70). Based on this, future comprehensive analyses should incorporate additional mechanistic experiments, such as immunoprecipitation and kinase activation assays, to further elucidate the crosstalk between HY-N7656 and upstream and downstream signaling involved in RILI (PI3K/Akt, Wnt/β-catenin and NF-κB pathways) (22).

To the best of the authors' knowledge, the present study is the first to demonstrate that the natural flavonoid, HY-N7656, may serve as a novel therapeutic agent for mitigating RILI. Results of the present study indicated that HY-N7656 targets the PI3K/Akt signaling pathway to suppress EMT progression, markedly reduced pulmonary inflammation and fibrosis, preserved epithelial integrity and ultimately ameliorated RILI. Future research should prioritize preclinical validation in humanized models and Phase I evaluation of its combinatorial potential with radiotherapy, offering a novel strategy for RILI treatment.

Acknowledgements

Not applicable.

Funding

The present study was supported by Sichuan Medical Association (grant no. 2024HR15), The Chengdu Technology Bureau Program (grant nos. 2024-YF05-02230-SN and 2024-YF05-01283-SN) and the Sichuan Provincial Administration of Traditional Chinese Medicine Project (grant no. 2023MS433).

Availability of data and materials

The data generated in the present study may be requested from the corresponding author.

Authors' contributions

CCG designed and conducted animal and cell experiments, processed the data and wrote the manuscript. HKL collated the experimental results, plotted charts and revised the

manuscript. YZM, JYC, ZYF, SLF and LQ were involved in the experimental process and data collection. BL, KX and MHC provided financial support. JYL and QC provided ideas for the design of the project. CCG and MHC confirm the authenticity of all the raw data. All authors read and approved the final manuscript.

Ethics approval and consent to participate

The animal experiments were approved by the Animal Ethics Committee of Sichuan Cancer Hospital (approval no. SCCHEC-04-2024-040).

Patient consent for publication

Not applicable.

Competing interests

The authors declare that they have no competing interests.

References

1. Xu T, Zhang Y, Chang P, Gong S, Shao L and Dong L: Mesenchymal stem cell-based therapy for radiation-induced lung injury. Stem Cell Res Ther 9: 18, 2018.
2. Bradley JD, Paulus R, Komaki R, Masters G, Blumenschein G, Schild S, Bogart J, Hu C, Forster K, Magliocco A, *et al*: Standard-dose versus high-dose conformal radiotherapy with concurrent and consolidation carboplatin plus paclitaxel with or without cetuximab for patients with stage IIIA or IIIB non-small-cell lung cancer (RTOG 0617): A randomised, two-by-two factorial phase 3 study. Lancet Oncol 16: 187-199, 2015.
3. Sharma GP, Fish BL, Frei AC, Narayanan J, Gasperetti T, Scholler D, Pierce L, Szalewski N, Blue N, Medhora M and Himburg HA: Pharmacologic ACE-inhibition mitigates radiation-induced pneumonitis by suppressing ACE-expressing lung myeloid cells. Int J Radiat Oncol Biol Phys 113: 177-191, 2022.
4. Onishi H, Marino K, Yamashita H, Terahara A, Onimaru R, Kokubo M, Shioyama Y, Kozuka T, Matsuo Y, Aruga T and Hiraoka M: Case series of 23 patients who developed fatal radiation pneumonitis after stereotactic body radiotherapy for lung cancer. Technol Cancer Res Treat 17: 1533033818801323, 2018.
5. Meng Y, Yang H, Wang W, Tang X, Jiang C, Shen Y and Luo W: Excluding PTV from lung volume may better predict radiation pneumonitis for intensity modulated radiation therapy in lung cancer patients. Radiat Oncol 14: 7, 2019.
6. Xu S, Liu C and Ji HL: Concise review: Therapeutic potential of the mesenchymal stem cell derived secretome and extracellular vesicles for radiation-induced lung injury: Progress and hypotheses. Stem Cells Transl Med 8: 344-354, 2019.
7. Giuranno L, Ient J, De Ruysscher D and Vooijs MA: Radiation-induced lung injury (RILI). Front Oncol 9: 877, 2019.
8. Bledsoe TJ, Nath SK and Decker RH: Radiation pneumonitis. Clin Chest Med 38: 201-208, 2017.
9. Deng Y, Xia X, Zhao Y, Zhao Z, Martinez C, Yin W, Yao J, Hang Q, Wu W, Zhang J, *et al*: Glucocorticoid receptor regulates PD-L1 and MHC-I in pancreatic cancer cells to promote immune evasion and immunotherapy resistance. Nat Commun 12: 7041, 2021.
10. Li L, Wu D, Deng S, Li J, Zhang F, Zou Y, Zhang T and Xu Y: NVP-AUY922 alleviates radiation-induced lung injury via inhibition of autophagy-dependent ferroptosis. Cell Death Discov 8: 86, 2022.
11. Simone CB II: Thoracic radiation normal tissue injury. Semin Radiat Oncol 27: 370-377, 2017.
12. Froese AR, Shimbori C, Bellaye PS, Inman M, Obex S, Fatima S, Jenkins G, Gauldie J, Ask K and Kodlb M: Stretch-induced activation of transforming growth factor-β1 in pulmonary fibrosis. Am J Respir Crit Care Med 194: 84-96, 2016.
13. Singh V, Torricelli AA, Nayeb-Hashemi N, Agrawal V and Wilson SE: Mouse strain variation in SMA(+) myofibroblast development after corneal injury. Exp Eye Res 115: 27-30, 2013.
14. Tatler AL and Jenkins G: TGF-β activation and lung fibrosis. Proc Am Thorac Soc 9: 130-136, 2012.
15. Kim KK, Kugler MC, Wolters PJ, Robillard L, Galvez MG, Brumwell AN, Sheppard D and Chapman HA: Alveolar epithelial cell mesenchymal transition develops in vivo during pulmonary fibrosis and is regulated by the extracellular matrix. Proc Natl Acad Sci USA 103: 13180-13185, 2006.
16. Park HR, Jo SK and Jung U: Ionizing radiation promotes epithelial-to-mesenchymal transition in lung epithelial cells by TGF-β-producing M2 macrophages. In Vivo 33: 1773-1784, 2019.
17. Sohn SH, Lee JM, Park S, Yoo H, Kang JW, Shin D, Jung KH, Lee YS, Cho J and Bae H: The inflammasome accelerates radiation-induced lung inflammation and fibrosis in mice. Environ Toxicol Pharmacol 39: 917-926, 2015.
18. Moghbeli M: PI3K/AKT pathway as a pivotal regulator of epithelial-mesenchymal transition in lung tumor cells. Cancer Cell Int 24: 165, 2024.
19. Bustamante A, Baritaki S, Zaravinos A and Bonavida B: Relationship of signaling pathways between RKIP expression and the inhibition of EMT-inducing transcription factors SNAIL1/2, TWIST1/2 and ZEB1/2. Cancers (Basel) 16: 3180, 2024.
20. Yan Z, Zhu J, Liu Y, Li Z, Liang X, Zhou S, Hou Y, Chen H, Zhou L, Wang P, *et al*: DNA-PKcs/AKT1 inhibits epithelial-mesenchymal transition during radiation-induced pulmonary fibrosis by inducing ubiquitination and degradation of Twist1. Clin Transl Med 14: e1690, 2024.
21. Conte E, Fruciano M, Fagone E, Gili E, Caraci F, Iemmolo M, Crimi N and Vancheri C: Inhibition of PI3K prevents the proliferation and differentiation of human lung fibroblasts into myofibroblasts: the role of class I P110 isoforms. PLoS One 6: e24663, 2011.
22. Zhang XL, Xing RG, Chen L, Liu CR and Miao ZG: PI3K/Akt signaling is involved in the pathogenesis of bleomycin-induced pulmonary fibrosis via regulation of epithelial-mesenchymal transition. Mol Med Rep 14: 5699-5706, 2016.
23. Wang B, Wei J, Meng L, Wang H, Qu C, Chen X, Xin Y and Jiang X: Advances in pathogenic mechanisms and management of radiation-induced fibrosis. Biomed Pharmacother 121: 109560, 2020.
24. Lin B, Zhang P and Lang J: Clinical observation of Huaxian decociton on preventing 70 cases of radio-pulmonarylesion. J Sichuan Tradit Chin Med 30: 76-78, 2012 (In Chinese).
25. Lin B, Zhang P and Lang J: Experimental research of using Huaxian decociton to prevent and treating radiation fibrosis of lung. J Sichuan Tradit Chin Med 33: 54-57, 2015 (In Chinese).
26. Chen J, Zou P, Fang Z, Gong C, Yin J, Chen M, Lin B and Lang J: Hua Xian Fang alleviates radiation-induced pulmonary fibrosis by upregulating the level of IFN-γ in blood and tissues. Chin J Radiat Oncol 33: 554-561, 2024 (In Chinese).
27. Chen J, Zou P, Quan L, Gong C, Fang Z, Lin B, Lang J and Chen M: Huaxian formula prevents the progression of radiation-induced pulmonary fibrosis by inhibiting the pro-fibrotic effects of macrophages. J Ethnopharmacol 338: 119026, 2025.
28. Gong C, Chen J, Zou P, Fang Z, Quan L, Wang J, Yin J, Lin B, Lang J and Chen M: Serum pharmacochemistry and network pharmacology reveal active compounds and mechanisms of the huaxian formula in alleviating radiation-induced pulmonary fibrosis. Drug Des Devel Ther 19: 627-644, 2025.
29. Shen DY, Juang SH, Kuo PC, Huang GJ, Chan YY, Damu AG and Wu TS: Chemical constituents from andrographis echioides and their anti-inflammatory activity. Int J Mol Sci 14: 496-514, 2012.
30. Travis EL, Rachakonda G, Zhou X, Korhonen K, Sekhar KR, Biswas S and Freeman ML: NRF2 deficiency reduces life span of mice administered thoracic irradiation. Free Radic Biol Med 51: 1175-1183, 2011.
31. Niu S, Zhang Y, Cong C, Wu Z, Wang Z, Sun M, Yao C and Zhang Y: Comparative study of radiation-induced lung injury model in two strains of mice. Health Phys 122: 579-585, 2022.
32. Lierova A, Kasparova J, Pejchal J, Kubelkova K, Jelicova M, Palarcik J, Korecka L, Bilkova Z and Sinkorova Z: Attenuation of radiation-induced lung injury by hyaluronic acid nanoparticles. Front Pharmacol 11: 1199, 2020.
33. Gattinoni L, Caironi P, Pelosi P and Goodman LR: What has computed tomography taught us about the acute respiratory distress syndrome? Am J Respir Crit Care Med 164: 1701-1711, 2001.
34. Szapiel SV, Elson NA, Fulmer JD, Hunninghake GW and Crystal RG: Bleomycin-induced interstitial pulmonary disease in the nude, athymic mouse. Am Rev Respir Dis 120: 893-899, 1979.

35. Hübner RH, Gitter W, El Mokhtari NE, Mathiak M, Both M, Bolte H, Freitag-Wolf S and Bewig B: Standardized quantification of pulmonary fibrosis in histological samples. Biotechniques 44: 507-511, 514-517, 2008.
36. Missiuro PV, Liu K, Zou L, Ross BC, Zhao G, Liu JS and Ge H: Information flow analysis of interactome networks. PLoS Comput Biol 5: e1000350, 2009.
37. Liu Y, Yang X, Gan J, Chen S, Xiao ZX and Cao Y: CB-Dock2: Improved protein-ligand blind docking by integrating cavity detection, docking and homologous template fitting. Nucleic Acids Res 50: W159-W164, 2022.
38. Livak KJ and Schmittgen TD: Analysis of relative gene expression data using real-time quantitative PCR and the 2(-delta delta C(T)) method. Methods 25: 402-408, 2001.
39. Kang SK, Rabbani ZN, Folz RJ, Golson ML, Huang H, Yu D, Samulski TS, Dewhirst MW, Anscher MS and Vujaskovic Z: Overexpression of extracellular superoxide dismutase protects mice from radiation-induced lung injury. Int J Radiat Oncol Biol Phys 57: 1056-1066, 2003.
40. Travis EL, Down JD, Holmes SJ and Hobson B: Radiation pneumonitis and fibrosis in mouse lung assayed by respiratory frequency and histology. Radiat Res 84: 133-143, 1980.
41. Li X, Ma L, Huang K, Wei Y, Long S, Liu Q, Zhang D, Wu S, Wang W, Yang G, *et al*: Regorafenib-attenuated, bleomycin-induced pulmonary fibrosis by inhibiting the TGF-β1 signaling pathway. Int J Mol Sci 22: 1985, 2021.
42. Yang K, Palm J, König J, Seeland U, Rosenkranz S, Feiden W, Rübe C and Rübe CE: Matrix-metallo-proteinases and their tissue inhibitors in radiation-induced lung injury. Int J Radiat Biol 83: 665-676, 2007.
43. Kim SB, Ly P, Kaisani A, Zhang L, Wright WE and Shay JW: Mitigation of radiation-induced damage by targeting EGFR in noncancerous human epithelial cells. Radiat Res 180: 259-267, 2013.
44. Chen ZY, Xiao HW, Dong JL, Li Y, Wang B, Fan SJ and Cui M: Gut microbiota-derived PGF2α fights against radiation-induced lung toxicity through the MAPK/NF-κB pathway. Antioxidants (Basel) 11: 65, 2021.
45. He G, Tang A, Xie M, Xia W, Zhao P, Wei J, Lai Y, Tang X, Zou YM and Liu H: Blood gene expression profile study revealed the activation of apoptosis and p53 signaling pathway may be the potential molecular mechanisms of ionizing radiation damage and radiation-induced bystander effects. Dose Response 18: 1559325820914184, 2020.
46. Lieverse RIY, Van Limbergen EJ, Oberije CJG, Troost EGC, Hadrup SR, Dingemans AC, Hendriks LEL, Eckert F, Hiley C, Dooms C, *et al*: Stereotactic ablative body radiotherapy (SABR) combined with immunotherapy (L19-IL2) versus standard of care in stage IV NSCLC patients, ImmunoSABR: A multicentre, randomised controlled open-label phase II trial. BMC Cancer 20: 557, 2020.
47. Hou G, Li J, Liu W, Wei J, Xin Y and Jiang X: Mesenchymal stem cells in radiation-induced lung injury: From mechanisms to therapeutic potential. Front Cell Dev Biol 10: 1100305, 2022.
48. Konkol M, Śniatała P and Milecki P: Radiation-induced lung injury - what do we know in the era of modern radiotherapy? Rep Pract Oncol Radiother 27: 552-565, 2022.
49. Drishya S, Dhanisha SS, Raghukumar P and Guruvayoorappan C: *Amomum subulatum* mitigates experimental thoracic radiation-induced lung injury by regulating antioxidant status and inflammatory responses. Food Funct 14: 1545-1559, 2023.
50. Fox MS, Ouriadov A, Thind K, Hegarty E, Wong E, Hope A and Santyr GE: Detection of radiation induced lung injury in rats using dynamic hyperpolarized (129)Xe magnetic resonance spectroscopy. Med Phys 41: 072302, 2014.
51. Kun C, Tao L, Leiyuan H, Yunhao F, Ning W, Zhe L, Yuanyuan C, Xiao L, Hongran Q, Jianming C, *et al*: Heat-killed Salmonella typhimurium mitigated radiation-induced lung injury. Clin Exp Pharmacol Physiol 46: 1084-1091, 2019.
52. Kim JS, Son Y, Jung MG, Jeong YJ, Kim SH, Lee SJ, Lee YJ and Lee HJ: Geranylgeranylacetone alleviates radiation-induced lung injury by inhibiting epithelial-to-mesenchymal transition signaling. Mol Med Rep 13: 4666-4670, 2016.
53. Wang X, Li M, Yin J, Fang J, Ying Y, Ye T, Zhang F, Ma S, Qin H and Liu X: Emetine dihydrochloride alleviated radiation-induced lung injury through inhibiting EMT. J Cell Mol Med 27: 3839-3850, 2023.
54. Lamouille S, Xu J and Derynck R: Molecular mechanisms of epithelial-mesenchymal transition. Nat Rev Mol Cell Biol 15: 178-196, 2014.
55. Nagaraja SS and Nagarajan D: Radiation-induced pulmonary epithelial-mesenchymal transition: A review on targeting molecular pathways and mediators. Curr Drug Targets 19: 1191-1204, 2018.
56. Qu H, Liu L, Liu Z, Qin H, Liao Z, Xia P, Yang Y, Li B, Gao F and Cai J: Blocking TBK1 alleviated radiation-induced pulmonary fibrosis and epithelial-mesenchymal transition through Akt-Erk inactivation. Exp Mol Med 51: 1-17, 2019.
57. Wang J, Bao L, Yu B, Liu Z, Han W, Deng C and Guo C: Interleukin-1β promotes epithelial-derived alveolar elastogenesis via αvβ6 integrin-dependent TGF-β activation. Cell Physiol Biochem 36: 2198-2216, 2015.
58. Wang M, Feng Y, Zhang P, Shen K, Su J, Zhong Y, Yang X, Lin S and Lu J: Jiawei Maxing Shigan Tang alleviates radiation-induced lung injury via TGF-β1/Smad signaling pathway mediated by regulatory T cells. J Ethnopharmacol 320: 117389, 2024.
59. Chen H, Chen N, Li F, Sun L, Du J, Chen Y, Cheng F, Li Y, Tian S, Jiang Q, *et al*: Repeated radon exposure induced lung injury and epithelial-mesenchymal transition through the PI3K/AKT/mTOR pathway in human bronchial epithelial cells and mice. Toxicol Lett 334: 4-13, 2020.
60. Polimeni M, Gulino GR, Gazzano E, Kopecka J, Marucco A, Fenoglio I, Cesano F, Campagnolo L, Magrini A, Pietroiusti A, *et al*: Multi-walled carbon nanotubes directly induce epithelial-mesenchymal transition in human bronchial epithelial cells via the TGF-β-mediated Akt/GSK-3β/SNAIL-1 signalling pathway. Part Fibre Toxicol 13: 27, 2016.
61. Qian W, Cai X, Qian Q, Zhang W and Wang D: Astragaloside IV modulates TGF-β1-dependent epithelial-mesenchymal transition in bleomycin-induced pulmonary fibrosis. J Cell Mol Med 22: 4354-4365, 2018.
62. Bakin AV, Tomlinson AK, Bhowmick NA, Moses HL and Arteaga CL: Phosphatidylinositol 3-kinase function is required for transforming growth factor beta-mediated epithelial to mesenchymal transition and cell migration. J Biol Chem 275: 36803-38610, 2000.
63. Li Y, Shen Z, Jiang X, Wang Y, Yang Z, Mao Y, Wu Z, Li G and Chen H: Mouse mesenchymal stem cell-derived exosomal miR-466f-3p reverses EMT process through inhibiting AKT/GSK3β pathway via c-MET in radiation-induced lung injury. J Exp Clin Cancer Res 41: 128, 2022.
64. Karimi Roshan M, Soltani A, Soleimani A, Rezaie Kahkhaie K, Afshari AR and Soukhtanloo M: Role of AKT and mTOR signaling pathways in the induction of epithelial-mesenchymal transition (EMT) process. Biochimie 165: 229-234, 2019.
65. Zhao DY, Qu HJ, Guo JM, Zhao HN, Yang YY, Zhang P, Cao K, Lei X, Cui JG, Liu C, *et al*: Protective effects of myrtol standardized against radiation-induced lung injury. Cell Physiol Biochem 38: 619-634, 2016.
66. Yang C, Song C, Wang Y, Zhou W, Zheng W, Zhou H, Deng G, Li H, Xiao W, Yang Z, *et al*: Re-Du-Ning injection ameliorates radiation-induced pneumonitis and fibrosis by inhibiting AIM2 inflammasome and epithelial-mesenchymal transition. Phytomedicine 102: 154184, 2022.
67. Liu X, Shao C and Fu J: Promising biomarkers of radiation-induced lung injury: A review. Biomedicines 9: 1181, 2021.
68. Wu N, Li Z, Wang J, Geng L, Yue Y, Deng Z, Wang Q and Zhang Q: Low molecular weight fucoidan attenuating pulmonary fibrosis by relieving inflammatory reaction and progression of epithelial-mesenchymal transition. Carbohydr Polym 273: 118567, 2021.
69. Yang M, Che Y, Li K, Fang Z, Li S, Wang M, Zhang Y, Xu Z, Luo L, Wu C, *et al*: [Detection and quantitative analysis of tumor-associated tertiary lymphoid structures]. J Zhejiang Univ Sci B 24: 779-795, 2023 (In English, Chinese).
70. Zhou X, Bao WA, Zhu X, Lin J, Fan JF, Yang Y, Du XH and Wang YZ: 3,3'-Diindolylmethane attenuates inflammation and fibrosis in radiation-induced lung injury by regulating NF-κB/TGF-β/Smad signaling pathways. Exp Lung Res 48: 103-113, 2022.